Battery-Health Conscious Power Management in Plug-In Hybrid Electric Vehicles via Electrochemical Modeling and Stochastic Control

Scott J. Moura, *Student Member, IEEE*, Jeffrey L. Stein, and Hosam K. Fathy

Abstract—This paper develops techniques to design plug-in hybrid electric vehicle (PHEV) power management algorithms that optimally balance lithium-ion battery pack health and energy consumption cost. As such, this research is the first to utilize electrochemical battery models to optimize the power management in PHEVs. Daily trip length distributions are integrated into the problem using Markov chains with absorbing states. We capture battery aging by integrating two example degradation models: solid–electrolyte interphase (SEI) film formation and the "Ah-processed" model. This enables us to optimally tradeoff energy cost versus battery-health. We analyze this tradeoff to explore how optimal control strategies and physical battery system properties are related. Specifically, we find that the slope and convexity properties of the health degradation model profoundly impact the optimal charge depletion strategy. For example, solutions that balance energy cost and SEI layer growth aggressively deplete battery charge at high states-of-charge (SoCs), then blend engine and battery power at lower SoCs.

Index Terms—Batteries, electrochemical modeling, optimal control, plug-in hybrid vehicles, power management, stochastic control.

I. INTRODUCTION

A. Motivation

THIS paper develops techniques to design supervisory control algorithms that manage the tradeoff between battery pack health and energy consumption cost in plug-in hybrid electric vehicles (PHEVs). The mechanisms responsible for battery degradation are widely-varying, complex, and not universally captured into one simple, accurate model [1]. As such, we pursue *techniques* for power management that incorporate a class of degradation models. This paper leverages both stochastic control theory and reduced electrochemical battery models to achieve its goal. Given experimentally validated degradation models, these algorithms have the potential to increase the useful life and long-term energy capacity of battery packs. This is critically important for large-scale battery energy storage systems - ranging from PHEVs to stationary grid-scale storage - where replacement cost, bulk, and cycle life are inhibiting factors associated with the uncertainty in maintaining safe operation. As such, this paper's overall goal is to design tools for solving power management algorithms that manage battery-health degradation in some optimal sense. We pursue this goal specifically for a power-split hybrid configuration with a battery pack consisting of lithium-ion cells. Moreover, daily trip length distributions are explicitly accounted for the problem formulation by applying Markov chains with absorbing states.

Managing degradation is particularly challenging for two reasons. First, the most critical damage mechanisms are still not fully understood. As such, we pursue power management formulation techniques that incorporate broad ranges of degradation models. Second, the dynamics are simulated using computationally intensive electrochemistry-based models that are inconducive to control design. This fact is underscored in the context of this paper, which leverages dynamic programming techniques and the associated "curse of dimensionality." Moreover, PHEV power management is, by itself, a nontrivial problem that requires the solution of an optimal control problem with multiple inputs, stochastic dynamics, state and control constraints. Therefore, we extend our previous research on PHEV power management [2], [3] and lithium-ion battery-health degradation simulation and model reduction [4] to solve the present problem with an electrochemical battery model. The resulting control algorithms tradeoff energy consumption cost with battery life by combining, for the first time, dynamic PHEV models, stochastic drive cycle models with trip length knowledge, and reduced electrochemical battery degradation models.

B. Summary of Prior Literature

Two general categories of research provide the background for battery-health conscious hybrid vehicle power management.

1) Electrochemical Battery Modeling: First, a large body of literature exists on modeling degradation in lithium-ion batteries, including phenomena such as solid–electrolyte interface (SEI) film formation [5], [6], lithium plating [7], thermal damage [8], and mechanical degradation [9], [10]. Excellent

reviews by Aurbach [6] and Hatzell [11] survey these various mechanisms in depth. The key challenge to developing a singular, comprehensive, experimentally valid degradation model is the shear multiplicity of complex and interconnected degradation phenomena. As such, we seek to develop *tools* for designing the power management algorithms for battery-health.

As a case study, we examine a model particularly well-suited for model reduction and control applications that account for lithium diffusion dynamics, intercalation kinetics, and electrochemical potentials developed by Doyle, Fuller, and Newman [12], [13]. Ramadass *et al.* [5] added a degradation component to this model by including an irreversible solvent reduction reaction at the anode-side SEI that generates a resistive film, which consumes cyclable lithium. This mechanism has been identified as one of the chief contributors to capacity and power fade, whose effect is also representative of other mechanisms. We also consider the so-called "Ah-processed" model, which has been empirically identified as an accurate representation of battery-health for LiFePO$_4$ cells under certain cycling conditions [14], [15]. Since accurate battery-health modeling is an ever-evolving field, we develop a battery-health-conscious power management framework that is adaptable to a class of models and investigate SEI layer growth and Ah-processed as two particular case studies in this paper.

2) Vehicle Power Management: The second relevant body of research considers the general HEV power management problem. A broad spectrum of optimal control techniques has been developed to solve the power management problem. Examples include equivalent consumption minimization strategy [16], model predictive control [17], deterministic dynamic programming [18], [19], and stochastic dynamic programming [2], [20]. These strategies are optimized for objectives, such as fuel consumption [16]–[20], emissions [21], drivability [22], and/or combined fuel/electricity consumption [2]. For PHEVs, several studies (e.g., [19] have identified that the optimal strategy rations battery charge such that it reaches the minimum value exactly when the trip terminates. However, exact *a priori* knowledge of drive cycle behavior and length is typically not available.

Our focus is to connect these two previously disparate bodies of literature. Specifically, we combine stochastic dynamic programming with degrading electrochemical battery models and distributions of daily trip lengths. Several more recent studies have considered the HEV power management problem for extending battery life. These studies focus on depth of discharge control [23], [24], power electronics management [25], and temperature management [26]. To present, however, no studies have applied models that explicitly account for specific electrochemical degradation mechanisms in the context of an optimal control framework, to the authors' knowledge.

C. Main Contributions of this Paper

The main goal of this paper is to extend and connect the above research on battery-health management and PHEV power management by adding three important and original contributions. First, we directly model daily vehicle trip lengths using a Markov chain with a terminal state, identified from real-world survey data. Second, we formulate a

TABLE I
GENERAL PHEV MODEL PARAMETERS

Vehicle	EPA classification	Midsize Sedan
	HEV configuration	Power-split
	Base curb Weight	1471 kg
Engine	Type	Gasoline Inline 4-cylinder
	Displacement	1.5 L
	Max power	57 kW @ 4500 RPM
	Max torque	110 N-m @ 4500 RPM
Machines	Type	Permanent Magnet AC
	M1 Max power	30 kW @ 3000–5500 RPM
	M2 Max power	35 kW @ 1040–5600 RPM
Battery pack	Cell chemistry	LiFePO$_4$
	Energy capacity	5 kWh for pack
	Charge capacity	2.3 Ah per cell
	Number of cells	660

multiobjective optimal control problem that seeks to manage power flow in a power-split PHEV to minimize both health degradation and energy consumption cost. Third, we analyze the fundamental tradeoffs between energy consumption cost and battery-health degradation for two important degradation models. This paper extends our previous work [3] by incorporating an electrochemical model into the control design process (Section II-B1) and studying the charge-processed degradation model (Section VI). The results of this research provide useful insight into health-conscious power management of lithium-ion battery storage systems.

D. Outline

The outline of this paper is as follows. Section II develops the system models, including the PHEV, battery, health degradation mechanisms, and drive cycle dynamics. Section III formulates the optimal control problem. Section IV describes the control synthesis and analysis procedure. Sections V and VI present and discuss the main results for the two respective case studies, SEI layer growth, and Ah-processed. Finally, Section VII summarizes this paper's main contributions and conclusions.

II. MODEL DEVELOPMENT

The PHEV modeled in this paper has a power-split configuration based upon THS-II [27], with a lithium-ion battery pack enlarged to a 5-kWh energy capacity for plug-in operation [28]. General parameters for the vehicle are provided in Table I. A schematic of the PHEV system, the supervisory controller, and the relevant signals is given in Fig. 1. The state variables include engine speed, vehicle speed, battery state-of-charge (SoC) and acceleration. Acceleration is governed by a Markov chain, which captures drive cycle dynamics, described in Section II-E. We design this Markov chain to explicitly account for real-world *daily* trip length distributions - which is relevant for PHEVs that will potentially recharge overnight. In addition, we also include a battery-health degradation model based upon an electrochemical anode-side film formation mechanism and Ah-processed. In the following sections, we summarize the dynamic phenomena and governing equations for these models. Please reference the nomenclature section in the appendix for variable definitions.

This article has been accepted for inclusion in a future issue of this journal. Content is final as presented, with the exception of pagination.

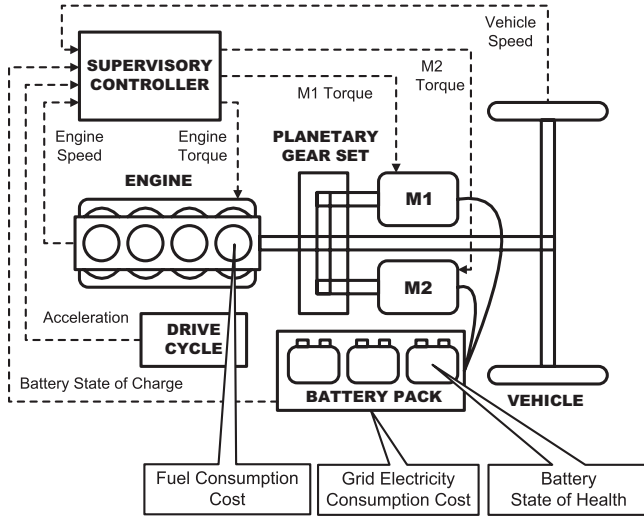MOURA *et al.*: BATTERY-HEALTH CONSCIOUS POWER MANAGEMENT IN PHEVs

3

Fig. 1. PHEV powertrain system model. The supervisory controller provides the optimal engine, M1, and M2 torque inputs as a function of the PHEV states to minimize energy consumption and battery degradation.

A. PHEV Model

1) Mechanical Subsystem: The planetary gear set is at the heart of the power-split configuration. This three-port device couples the engine, machine 1 (M1), and machine 2 (M2) crankshafts. The dynamic-algebraic equations, that describe this device, are governed by Euler's law and a kinematic constraint relating component speeds [29]

$$
\begin{bmatrix}
I_e & 0 & 0 & R+S \\
0 & I_{M1} & 0 & -S \\
0 & 0 & I'_{M2} & -R \\
R+S & -S & -R & 0
\end{bmatrix}
\begin{bmatrix}
\dot{\omega}_e \\
\dot{\omega}_{M1} \\
\dot{\omega}_{M2} \\
F_g
\end{bmatrix}
=
\begin{bmatrix}
T_e \\
T_{M1} \\
T'_{M2} \\
0
\end{bmatrix}. \quad (1)
$$

The terms I'_{M2} and T'_{M2} are effective inertia and torques

$$
I'_{M2} = \frac{I_{M2} + (I_w + mR_{\text{tire}}^2)}{K^2} \quad (2)
$$

$$
T'_{M2} = \frac{T_{M2} + F_{\text{road}}R_{\text{tire}}}{K} \quad (3)
$$

$$
F_{\text{road}} = 0.5\rho C_d A_{\text{fr}} v^2 + \mu_{\text{roll}} mg \quad (4)
$$

where F_{road} includes viscous aerodynamic drag and rolling friction forces.

Liu [29] demonstrated that the differential-algebraic equations that govern all possible power-split designs satisfy a universal matrix format. This format has the special property that one may analytically solve for the state variables without explicitly determining the gear force F or inverting the matrix on the LHS of (1). This process results in two degrees-of-freedom, since there exist three ordinary differential equations and one algebraic constraint.

The control inputs include engine torque T_e and M1 torque T_{M1}. The engine is allowed to shutoff by considering an "engine off" torque input command, which causes the engine speed to drop to zero within the span of one supervisory control time step (one second in this case). When positive torque is commanded from the engine while it is in the shutoff state, the engine is brought back to idle speed within one

supervisory control time step. During both engine-on and engine-off modes, and transitions in between, the equations in (1)–(4) must be respected. For example, $\dot{\omega}_e = 0$ when the engine remains off. When the engine is commanded to turn on, then $\dot{\omega}_e$ must equal the appropriate value such that it reaches idle speed in the next simulation time step. M2 torque T_{M2} is determined by the states and control inputs, since $\dot{\omega}_{M2}$ is proportional to the acceleration state a according to $\dot{\omega}_{M2} = aK/R_{\text{tire}}$. Complete details on the modeling of engine startup and shutdown are described in [30].

2) Electric Subsystem: Both M1 and M2 interface with the battery pack, as shown in Fig. 1. These devices are modeled by power efficiency maps supplied by the Argonne National Laboratory's Powertrain System Analysis Toolkit [31]. The machine inertial dynamics are accounted for in (1), while their significantly faster inductive dynamics are approximated as instantaneous. The electrical powertrain also consists of power electronics. However, their dynamics are also ignored since they exceed the 1-Hz bandwidth typically considered in power management studies. Nonetheless, their power transfer losses are accounted for in the machine efficiency maps. Hence, the governing equations for the electric subsystem are given by

$$
P_{\text{batt}} = T_{M1}\omega_{M1}\eta_{M1}^{k_{M1}} + T_{M2}\omega_{M2}\eta_{M2}^{k_{M2}} \quad (5)
$$

$$
k_i = \begin{cases} -1, & T_i\omega_i > 0 \\ 1, & T_i\omega_i \le 0 \end{cases} \quad \text{for} \quad i = \{M1, M2\}. \quad (6)
$$

B. Battery Models

Two battery models are considered in the control design and analysis process. A high-fidelity electrochemical-based model is used for constraint satisfaction and closed-loop simulation. A low-order equivalent circuit model is used for control optimization, since it has one state variable. The parameters of both models have been identified experimentally on a custom-built hardware-in-the-loop setup, for commercial Li-ion cells containing LiFePO$_4$ cathode chemistries [32]. Interested readers may refer to [33] for further details on the genetic optimization procedure used to identify the parameters of the electrochemical model. In the following, we summarize the electrochemical battery model and equivalent circuit model.

1) Electrochemical Battery Model: The electrochemical battery model captures the spatiotemporal dynamics of lithium-ion concentration, electrode potential in each phase, and the Butler–Volmer kinetics that govern the intercalation reactions. A schematic of the model is provided in Fig. 2. This cross section displays three regions: a negative electrode (typically a lithium-carbon material), the separator, and a positive electrode (typically a lithium-metal-oxide). Each region is denoted by the subscript $j \in \{n, s, p\}$ representing the negative electrode, separator, and positive electrode, respectively. The positive electrode material varies widely across manufacturer designs. However, lithium iron phosphate (LiFePO$_4$) cells were used to identify this electrochemical model. Each electrode region contains two phases, the porous solid and electrolyte. The separator has an electrolyte phase only.

This article has been accepted for inclusion in a future issue of this journal. Content is final as presented, with the exception of pagination.

4   IEEE TRANSACTIONS ON CONTROL SYSTEMS TECHNOLOGY
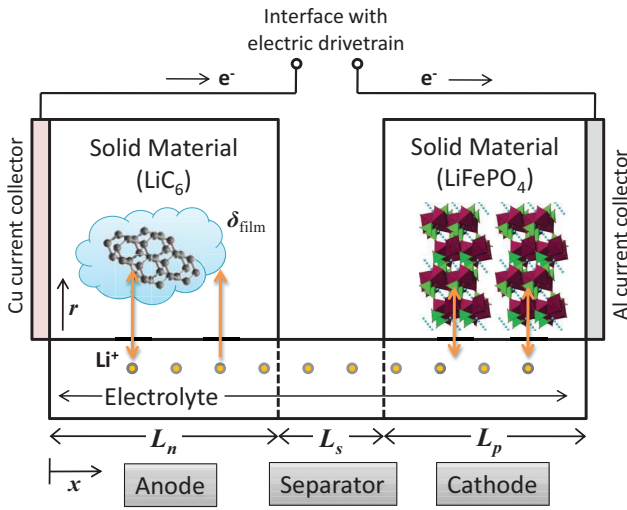

Fig. 2.   Structure of the electrochemical lithium-ion battery cell model.

Mathematically, the electrochemical model structure is a coupled set of partial differential-algebraic equations. Diffusion of lithium ions in the solid $c_{1,j}(r,t)$ is idealized by spherical diffusion. Diffusion of lithium ions across the electrolyte $c_{2,j}(x,t)$ is modeled by linear diffusion. Respectively, these phenomena are represented mathematically by

$$\frac{\partial c_{1,j}(r,t)}{\partial t} = \frac{D_{1,j}}{r^2}\frac{\partial}{\partial r}\left(r^2\frac{\partial c_{1,j}}{\partial r}\right) \tag{7}$$

$$\epsilon_{2,j}\frac{\partial c_{2,j}(x,t)}{\partial t} = D_2^{eff}\frac{\partial^2 c_{2,j}}{\partial x^2} + \frac{1-t^+}{F}J_j \tag{8}$$

where the variable J_j represents the local volumetric transfer current density due to Li-ion intercalation at the SEI.

The electric potential of each phase (solid: $\phi_{1,j}$, electrolyte: $\phi_{2,j}$) within each region is determined by a parameter-distributed form of Ohm's law. In the solid and electrolyte, this is given, respectively, by

$$J_j(x,t) = \frac{\partial}{\partial x}\left(\sigma_j^{eff}\frac{\partial\phi_{1,j}}{\partial x}\right) \tag{9}$$

$$J_j(x,t) = \frac{\partial}{\partial x}\left(\kappa^{eff}\frac{\partial\phi_{2,j}}{\partial x}\right) + \frac{\partial}{\partial x}\left(\kappa\frac{\partial\ln c_{2,j}}{\partial x}\right). \tag{10}$$

The first terms in each equation above represent the flux due to potential gradients. The second term in (10) represents the flux due to ionic concentration gradients in the electrolyte.

The intercalation current J_j is governed by Butler–Volmer kinetics in (11), where η_j is the local overpotential defined by (12)

$$J_j(x,t) = a_j i_{0,j}\sinh\left(\frac{\alpha_{a,j}F}{R_{gas}T}\eta_j\right) \tag{11}$$

$$\eta_j(x,t) = \phi_{1,j} - \phi_{2,j} - U_{ref,j}(\theta_j) - \frac{J_j}{a_n}R_{film}. \tag{12}$$

The term $U_{ref,j}$ is the reference potential of the corresponding electrode, and is a function of the bulk electrode SoC θ_j. Note that many comparable models utilize surface SoC as the argument for reference potential [34]–[37]. Extensive simulation analysis reveals this ultimately produces negligible difference in cell voltage within the allowable PHEV SoC range considered here: ($0.25 \leq$ SoC ≤ 0.95). From a supervisory control

systems perspective, we define the total battery SoC to be the spatially averaged SoC of the anode.

The model causality (i.e., input/output variables) is determined by the boundary conditions. For example, in galvanostatic mode, the input to this model is current $I(t)$, which enters as a Neumann boundary condition on the solid potential at the current collectors, as shown in (13). The output is terminal voltage $V_{cell}(t)$, given by the potential difference between the cathode and anode at the current collectors, as shown in (14)

$$I(t) = -A\sigma^{eff}\left.\frac{\partial\phi_1}{\partial x}\right|_{x=0} = A\sigma^{eff}\left.\frac{\partial\phi_1}{\partial x}\right|_{x=L} \tag{13}$$

$$V_{cell}(t) = \phi_1(L,t) - \phi_1(0,t). \tag{14}$$

In potentiostatic mode, voltage serves as the input by applying (14) as the boundary condition and measuring (13) as the output. In this manner, the causality can be switched according to which boundary condition is externally defined.

Numerically, the model is solved by the following four steps.

1) Represent the solid diffusion PDEs (7) using Padé approximation, which reduces the model dynamic order.
2) Quasilinearize the nonlinear Butler–Volmer equation (11) around the overpotential at each time step, which reduces the index order.
3) Represent all PDEs as a set of ODEs using finite differences.
4) Solve the resulting system of linear differential-algebraic equations. Readers interested in the complete details of the electrochemical battery model reduction and numerical solution should consult [33], [38].

2) Equivalent Circuit Model: Although the electrochemical model accurately predicts the spatiotemporal concentration and potential dynamics of a battery cell, its complex structure is not easily conducive to optimal control. This fact motivates the use of a reduced equivalent circuit model with a single state. This model idealizes the battery as an open-circuit voltage source in series with an internal resistance. Both electrical elements are continuous functions of SoC. Electric power at the battery terminals P_{batt} is the input. The conservation of power law indicates

$$V_{oc}I = I^2 R_{batt} + P_{batt} \tag{15}$$

and current is related to SoC through an integrator $\dot{SoC} = -I/Q_{batt}$. Using the quadratic equation results in the following dynamical battery systems:

$$\dot{SoC} = -\frac{V_{oc} - \sqrt{V_{oc}^2 - 4P_{batt}R_{batt}}}{2Q_{batt}R_{batt}}. \tag{16}$$

Note that (15) has two solutions for I. However, only one of these two solutions is physically feasible for negative power demands and provides the desired current with minimal resistive losses for nonnegative power demands. We, therefore, adopt this unique solution for battery current in (16).

To calculate the current I and voltage V_{cell} across each cell, one must know the battery pack configuration. That is, how many cells are arranged in series to produce the

desired pack voltage, and how many parallel strings exist to achieve the desired energy capacity. Here, we assume the use of 2.3 Ah 26650 format cells to be consistent with the experimental batteries used to identify the parameters of the electrochemical model in Section II-B1 (see [33] for details on the parameter identification process). The battery pack consists of $n_s = 110$ cells in series, and $n_p = 6$ parallel strings

$$I = \frac{\dot{\text{SoC}} \cdot Q_{\text{batt}}}{n_p} \qquad (17)$$

$$V_{\text{cell}} = \frac{(V_{\text{oc}} - I R_{\text{batt}})}{n_s}. \qquad (18)$$

Each cell is assumed to be identical or properly balanced through appropriate charge equalization schemes [39]. The current through each cell is used to calculate the anode-side film growth rate discussed in Section II-C. The voltage calculation is used to ensure each cell does not exceed safe operating limits - which we implement mathematically as constraints in the problem formulation in Section III.

Temperature dynamics and their impact on battery-health is also a critical factor to consider [40]–[42]. In this paper, we constrain the scope to batteries whose temperature is controlled around 25 °C through appropriate thermal management systems. Future work will investigate thermal estimation [43] and supervisory control strategies, which split power among the electric machines and cooling systems using coupled thermal-electrochemical battery models.

C. Anode-Side SEI Growth Model of Battery Aging

One important degradation mechanism that impacts battery-health is the formation of a resistive film at the SEI in the anode [5], [6], [44]. This mechanism effectively consumes cyclable lithium ions and increases the internal impedance. The exact chemical-side reaction depends on the chemistry of the electrode and electrolyte. Equations (19)–(24), developed by Ramadass *et al.* [5] argue that a simple and general method for modeling capacity loss is to assume an irreversible solvent reduction reaction of the following form:

$$S + Li^+ + e^- \rightarrow P \qquad (19)$$
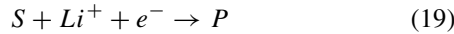
where S denotes the solvent species and P is the product.

As a result of this irreversible-side reaction, the products form a film at the solid/electrolyte interface, which has a time and spatially varying thickness $\delta_{\text{film}}(x, t)$ across the anode. This irreversibly formed film combines with the SEI resistance R_{SEI} to compose the total resistance at the SEI as follows:

$$R_{\text{film}}(x, t) = R_{\text{SEI}} + \frac{\delta_{\text{film}}(x, t)}{\kappa_P} \qquad (20)$$

where κ_P, denotes the conductivity of the film, x is the spatial coordinate, and t is time. The state equation corresponding to the growth of film thickness, due to the unwanted solvent reduction described in (19), is given by

$$\frac{\partial \delta_{\text{film}}(x, t)}{\partial t} = -\frac{M_P}{a_n \rho_P F} J_{sd}(x, t). \qquad (21)$$

In (21), M_P, a_n, ρ_P, and F represent the product's molecular weight, specific surface area, mass density, and Faraday's constant, respectively. The term J_{sd} denotes the local volumetric current density for the side reaction, which is governed by Butler–Volmer kinetics. If the solvent reduction reaction is irreversible and the variation of Li-ion concentration in the electrolyte is small, then we may approximate J_{sd} by the Tafel equation [45]

$$J_{\text{sd}}(x, t) = -i_{0,s} a_n e^{\left(\frac{-0.5F}{R_{\text{gas}}T} \eta_{\text{sd}}(x,t) \right)}. \qquad (22)$$

In (22), $i_{0,s}$, R, and T, respectively, denote the exchange current density for the side reaction, universal gas constant, and cell temperature. The term η_{sd} represents the side reaction overpotential, which drives the solvent reduction reaction in (19). The overpotential is calculated according to

$$\eta_{\text{sd}}(x, t) = \phi_1(x, t) - \phi_2(x, t) - U_{\text{ref},s} - \frac{J_{\text{tot}}(x, t)}{a_n} R_{\text{film}}(x, t). \qquad (23)$$

The variables ϕ_1 and ϕ_2 represent solid and electrolyte potentials, respectively. The symbol $U_{\text{ref},s}$ denotes the equilibrium potential of the solvent reduction reaction, which we assume to be constant. The total intercalation current J_{tot} represents the flow of charge exchanged with the anode-side electrolyte. Specifically, the total intercalation current J_n in the anode is given by the sum of current between the solid and electrolyte (J_1), and the solvent reduction reaction and electrolyte (J_{sd}), that is

$$J_{\text{tot}} = J_n + J_{\text{sd}}. \qquad (24)$$

Equations (20)–(24) encompass the film growth subsystem of the Li-ion battery cell model, adopted from [5]. This subsystem connects to the remainder of the battery model (7)–(14) through the total intercalation current J_n and potentials ϕ_1 and ϕ_2.

Although this model captures complex physical phenomena, such as coupled diffusion, intercalation, and film growth processes, its complexity makes control design for health management difficult. Therefore, the present research seeks to use the high fidelity model to generate simpler models for the purposes of control design. In the following, the anode-side film growth degradation dynamics will be approximated by a nonlinear static function, which enables optimal control design. Once the optimal control laws are derived from this approximate model, we simulate the closed-loop system with the full electrochemical model.

To acquire insight on the relationship between battery cell SoC, current, and film growth rate, consider an ideal fresh cell, that is $\delta_{\text{film}}(x, 0) = 0$. Suppose all the intercalation currents, overpotentials, and concentration profiles are constant with respect to space and correspond to zero initial applied current. Starting from these initial conditions, we simulate the electrochemical battery cell model for different initial SoCs and applied current levels and measure the instantaneous film growth rate. From this data, we produce a static relationship mapping cell SoC and applied current to the spatially averaged film growth rate $\dot{\bar{\delta}}_{\text{film}}$, shown in Fig. 3. This particular model was derived from previously reported experimental results in
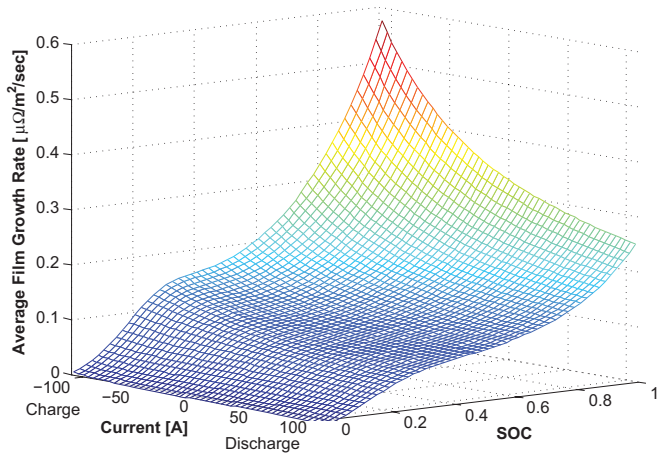
Fig. 3. Static approximation of film growth rate versus battery pack current and SoC utilized for PHEV power management control synthesis.

TABLE II

CYCLING CONDITIONS FOR EXPERIMENTAL STUDIES ON C-LiFePO$_4$ CELLS RELATING Ah-PROCESSED AND CAPACITY FADE

Reference	C-rate	Depth of discharge	Temperature
Peterson *et al.* [14]	Scaled PHEV drive cycle loads with C-rates ranging from $-3C$ to $+1C$	34 to 97%	Ambient room temp. (24–27 °C)
Wang *et al.* [15]	Constant current at C/2	10 to 90%	60 °C

the literature [5]; however, the authors are currently pursuing their own models from experimentally obtained empirical data. The map indicates that film growth rate increases with cell SoC. The film growth rate also increases as the discharge current becomes increasingly negative, i.e., for increasing charge current. Finally, film grows when zero current is applied, indicating that aging occurs even when the cells are not in use - a fact previously reported in the literature [44] and commonly seen in practice. A key question, we revisit after obtaining the optimal control solutions is what insight about the structural properties of this map can be leveraged to design supervisory power management controllers that reduce film formation in PHEV battery packs?

D. Charge-Processed Model of Battery Aging

In this section, we consider battery-health degradation in terms of a commonly seen empirical result found in numerous experimental studies [14], [15]. Specifically, this model assumes battery SOH degrades in direct proportion to the "charge-processed" through the battery. Physically, this implies that capacity fade mechanisms are insensitive to local SoC levels, depth of discharge, or electrode lithiation rates. Instead, these mechanisms progress in proportion with the integrated number of lithium ions intercalated or de-intercalated into the electrode. Generally speaking, this model suggests batteries degrade as their "mileage" increases. Mathematically, this means

$$\text{Capacity/Power Fade} \propto \int_{\tau=0}^{t} |I(\tau)| \, d\tau. \qquad (25)$$

Both experimental studies [14] and [15] utilized C-LiFePO$_4$ cells, which is the chemistry we mostly focus on in this paper. However, they also cycled these cells under relatively mild conditions. These conditions are summarized in Table II. In this table, one can see that Peterson *et al.* [14] applied scaled PHEV driving cycle loads. However, these loads were limited between $-3C$ and $+1C$, which is significantly less than the 30C maximum continuous discharge rate quoted by the manufacturer [32]. Low C-rates (namely C/2) also characterize the experimental results found by Wang *et al.* [15], which use

cells from the same manufacturer. In contrast to the first investigation, this paper cycled the cells at an elevated temperature of 60 °C, which will induce accelerated capacity fade.

Although, it remains an open question whether capacity fade is correlated with SoC or depth of discharge for high C-rates, we consider Ah-processed as a very simple model for battery-health degradation. That is, in Section VI we design PHEV supervisory control algorithms which optimally blend fuel and battery energy in a manner that minimizes the total Ah-processed through each cell.

E. Drive Cycle Model

An important new contribution, we apply toward *plug-in* HEV power management is to model drive cycles with a first-order Markov chain *containing a terminal state*. Namely, the terminal state can represent "vehicle off," which signifies when the drive cycle terminates and no more cost accrues. This allows us to model distributions of drive cycle length directly. As demonstrated by O'Keefe and Markel [19], drive cycle length is critically important for the *plug-in* HEV power management. They demonstrate that the optimal strategy rations battery charge through blending engine and battery power such that SoC reaches the minimum level exactly when the trip terminates, if the drive cycle is known *a priori*. This is in contrast to HEV power management, where battery SoC is typically sustained around a fixed value. This modeling approach is not new, and has been applied in the context of HEV power management [22]. Yet, its utility is particularly well suited for plug-in applications.

Mathematically, the Markov chain is given by

$$p_{\text{ijm}} = \Pr(a_{k+1} = j | a_k = i, v_k = m) \qquad (26)$$

$$p_{\text{itm}} = \Pr(a_{k+1} = t | a_k = i, v_k = 0) \qquad (27)$$

$$1 = \Pr(a_{k+1} = t | a_k = t, v_k = 0) \qquad (28)$$

which maps acceleration-velocity pairs to a probability distribution over acceleration in the next time step (26), (27). These transition probabilities are identified from certification cycles and real-world micro-trip data [2]. Fig. 4 visually demonstrates the transition probabilities at zero vehicle speed where there exists non-zero transition probabilities to the absorbing state for certain velocity-acceleration pairs. When acceleration reaches the terminal state t, it remains in that state with probability one (28) and no further cost is incurred. In other words, the vehicle is off and the trip is over.
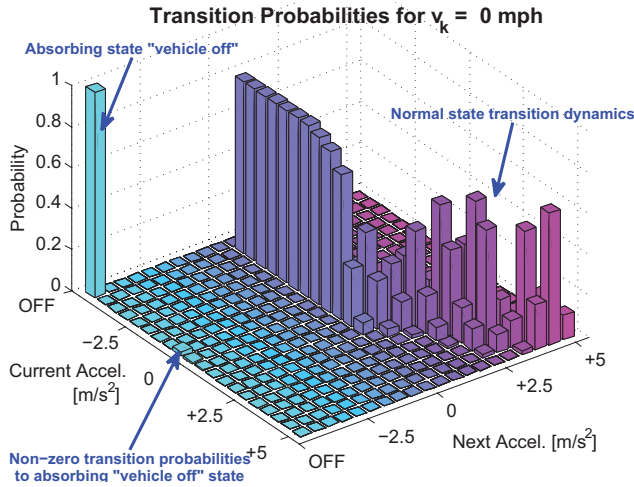
This article has been accepted for inclusion in a future issue of this journal. Content is final as presented, with the exception of pagination.

MOURA *et al.*: BATTERY-HEALTH CONSCIOUS POWER MANAGEMENT IN PHEVs

7

Fig. 4. Transition probabilities of the Markov chain for zero vehicle speed, which demonstrate the transition dynamics to the absorbing "vehicle off" state. The value of these transition probabilities relates to the distribution of daily trip length.

Fig. 5 demonstrates the distribution of trip length for the Markov chain, in which the transition probabilities p_{itm} in (27) have been optimized to fit data from the 2009 National Household Travel Survey (NHTS) [46]. Specifically, the probability of transition to "vehicle off" is zero unless the vehicle is completely stopped ($v_k = 0$) and has zero or small negative acceleration. Indeed, it is not possible to match the Markov chain to an arbitrary distribution of trip length without adding distance as a state (note some modeling error for low-trip lengths). If a distance-state variable was added, then it would produce an exponential increase in computational complexity. This approach integrates a reasonably accurate representation of real-world trip lengths without requiring an extra state - a key benefit.

In the main results presented in Sections V and VI, we evaluate each controller across a library of 1000 drive cycles generated from the Markov chain. This process enables us to quantify the performance metrics across a distribution of drive cycle characteristics, rather than single certification cycles.

III. OPTIMAL CONTROL PROBLEM FORMULATION

The control objective is to synthesize a static function, which maps the PHEV state variables to the engine and M1 torque inputs such that both energy consumption cost (i.e., fuel and grid electricity) and battery-health degradation are minimized. We formulate this as a shortest-path[1] stochastic dynamic programming problem

$$\text{min:} \quad J^g = \lim_{N \to \infty} \mathrm{E}\left[\sum_{k=0}^{N} c(x_k, u_k) \Delta t \right] \quad (29)$$

$$\text{s.t.} \quad x_{k+1} = f(x_k, u_k, w_k) \quad (30)$$

$$x \in X \quad (31)$$

$$u \in U(x) \quad (32)$$

[1]The shortest-path term [47] is used for Markov decision processes that contain a terminal state in the Markov chain, such as our drive cycle model.
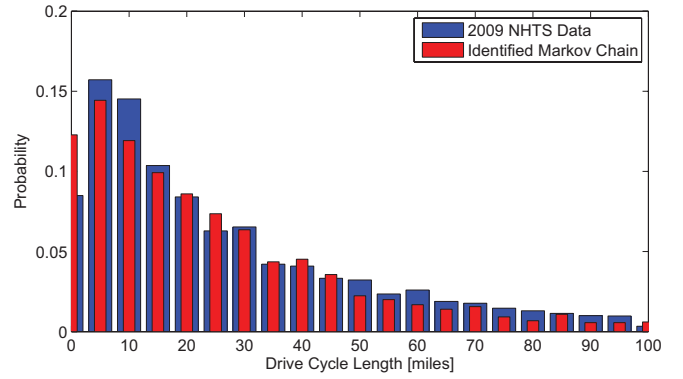

Fig. 5. Trip length distribution for 2009 NHTS data and the identified Markov chain.

where J^g is the cost for a given control policy g, $c(x_k, u_k)$ is a function that maps the state and control vectors to an instantaneous cost, and Δt is the time step size. The system dynamics summarized in discrete-time by (30) are provided in Section II, with a one-second time step ($\Delta t = 1$). This optimization is subject to sets of state and control constraints, X and $U(x)$, respectively, described in detail in Section III-B. Our objective is to solve for the optimal control policy g^*, which satisfies

$$g^* = \arg \inf_{g \in \mathcal{G}} J^g \quad (33)$$

where $\mathcal{G}$ denotes the set of all feasible control policies.

A. Objective Function

The minimization of the both energy consumption cost and battery-health is, generally speaking, a multiobjective optimal control problem. For simplicity, we combine both objectives into a scalar objective with linear weighting α, given mathematically by

$$c(x_k, u_k) = \alpha \cdot c_E(x_k, u_k) + (1 - \alpha) \cdot c_H(x_k, u_k) + c_{\text{SoC}}(x_k) \quad (34)$$

where the individual objective functions are given by

$$c_E(x_k, u_k) = \beta W_{\text{fuel}} + \frac{-V_{\text{oc}} Q_{\text{batt}} \dot{\text{SoC}}}{\eta_{\text{EVSE}}} \quad (35)$$

$$c_H(x_k, u_k) = \dot{\delta}_{\text{film}}(I, \text{SoC}) \quad \text{OR} \quad \left| \frac{I}{I_{\text{max}}} \right| \quad (36)$$

$$c_{\text{SoC}}(x_k) = \begin{cases} \frac{\alpha_{\text{SoC}}(\text{SoC}_{\text{cs}} - \text{SoC})}{\text{SoC}_{\text{max}} - \text{SoC}_{\text{cs}}}, & \text{SoC} \leq \text{SoC}_{\text{cs}} \\ 0, & \text{else.} \end{cases} \quad (37)$$

Equation (35) represents the instantaneous energy consumption cost in USD, which includes both fuel and grid charging costs. The first term of (35) quantifies PHEV fuel consumption, while the second term quantifies electricity consumption, both in terms of MJ per time step. The coefficient β makes it possible to carefully study tradeoffs between the two. Specifically, W_{fuel} represents the fuel consumption rate in grams per time step. Similarly, the second term of (35) represents the instantaneous rate of change of the battery's internal energy. Dividing this change in stored battery energy by a constant charging efficiency $\eta_{\text{EVSE}} = 0.98$

This article has been accepted for inclusion in a future issue of this journal. Content is final as presented, with the exception of pagination.

8   IEEE TRANSACTIONS ON CONTROL SYSTEMS TECHNOLOGY

(which represents losses from the power electronics in the electric vehicle supply equipment) furnishes an estimate of the amount of energy needed from the grid to replenish the battery charge consumed during the trip. Note that the second term is positive when the PHEV uses stored battery energy and negative during regeneration. Hence, there exists a reward for regeneration that offsets the need to consume grid electricity. The magnitude of this reward depends on the parameter β, which represents the relative price of gasoline per MJ to the price of grid electricity per MJ is defined as follows:

$$\beta = \frac{\text{Price of Gasoline per MJ}}{\text{Price of Grid Electricity per MJ}}. \tag{38}$$

We refer to this parameter as the "energy price ratio," and use it to examine the tradeoffs between fuel consumption and electricity consumption in PHEVs. Throughout this paper, we use $\beta = 0.8$, consistent with the average energy prices in June 2010, namely \$2.73 USD per gallon of gasoline [48] and \$0.094 USD per kWh of electricity [49].

Equation (36) represents one of the two types of battery-health models: the instantaneous anode-side SEI film growth, characterized by the map depicted in Fig. 3, or the normalized magnitude of applied current in a single battery cell. In the following sections, we consider PHEV power management controllers that minimize both of these measures of health degradation. In principle, other degradation models may also be included here. Additionally, both objectives are normalized by scaling the range of their natural values to values between zero and one.

Equation (37) invokes a linear penalty when the SoC falls below the charge sustaining threshold, SoC_{cs}. The parameter α_{SoC} is a penalty weight. The inclusion of this term produces the charge sustaining behavior, we desire once the minimum SoC value is reached.

We vary the weighting α in (34) between zero and one to obtain the convex subset of the Pareto optimal control policies. The complete Pareto optimal set would require multiobjective dynamic programming techniques, such as those developed in [50]. Henceforth, we refer to the convex subset of Pareto optimal solutions as, simply, the Pareto set - although this is admittedly an abuse of terminology.

B. Constraints

In addition to minimizing the aforementioned objectives, the power management algorithm satisfies constraints on both the states and control actions. These constraints correspond to physical operating limits, zones of safe operation, and actuation limits. Rate of change constraints are not considered here, although they can be easily added in this formulation. The state constraints are given by

$$\omega_{e,\min}(T_e) \leq \omega_e \leq \omega_{e,\max} \tag{39}$$

$$\omega_{M1,\min} \leq \omega_{M1} \leq \omega_{M1,\max} \tag{40}$$

$$\omega_{M2,\min} \leq \omega_{M2} \leq \omega_{M2,\max} \tag{41}$$

$$\text{SoC}_{\min} \leq \text{SoC} \leq \text{SoC}_{\max}. \tag{42}$$

Minimum engine speed is equal to idle speed when the engine is on, which is typically enforced for combustion stability,

noise, vibration, and harshness. Minimum engine speed is zero otherwise. The minimum M1 speed constraint also produces an interesting effect in a power-split configuration. If the engine is off, then ω_{M1} will violate its minimum value if vehicle speed, which is proportional to ω_{M2}, is sufficiently high, due to the kinematic relationship in (1). Consequently the engine must turn on for vehicle speeds greater than 36 mph, even when sufficient battery charge exists to run in all-electric mode. This constraint partly motivates the need for a dual-model power-split where all-electric operation is possible at high speeds [29].

The control constraints are given by the following:

$$T_{e,\min} \leq T_e \leq T_{e,\max}(\omega_e) \tag{43}$$

$$T_{M1,\min}(\omega_{M1}) \leq T_{M1} \leq T_{M1,\max}(\omega_{M1}) \tag{44}$$

$$T_{M2,\min}(\omega_{M2}) \leq T_{M2} \leq T_{M2,\max}(\omega_{M2}) \tag{45}$$

$$V_{\text{cell},\min} \leq V_{\text{cell}} \leq V_{\text{cell},\max} \tag{46}$$

$$I_{\text{cell},\min} \leq I_{\text{cell}} \leq I_{\text{cell},\max}. \tag{47}$$

The minimum M2 torque is determined by two constraints: saturation limits on M2 and the maximum battery pack voltage, which can be violated if too much regenerative power is supplied to the battery at, for example, high SoC levels. Hence, the minimum M2 torque is a function of several states and control inputs $T_{M2,\min} = T_{M2,\min}(\text{SoC}, \omega_{M1}, T_{M1}, \omega_{M2})$. The residual M2 torque after applying these constraints is provided by hydraulic braking.

To enforce both the state and control constraints, we apply the following methods. For all state and control pairs, we simulate the subsequent state using (30) and the full electrochemical model. If any constraints are violated then the corresponding control inputs are removed from the set of admissible controls, for the given state. This process generates the set of admissible controls $U(x)$ for each state, which can be computed offline from the stochastic dynamic programming algorithm, as described in Section IV.

C. Numerical Techniques

This section presents the numerical techniques used to derive the SDP feedback controllers.

The SDP problem, which is framed as an infinite-horizon shortest-path problem, is solved via modified policy iteration, where the policy evaluation step is approximated through successive value iterations. This algorithm has the property that convergence to the optimal policy occurs in finite time [47]. The approach begins with a uniform discretization of the admissible state and control input sets, X and $U(x)$. This discretization makes the optimal power management problem amenable to computer calculations, but generally produces suboptimal results. For a very thorough study of various discretization techniques, interested readers are referred to [51]. We use the symbols X and $U(x)$ to refer to both the continuous- and discrete-valued state and control input sets for ease of reading. Given the discrete-valued sets, we apply a modified policy iteration algorithm to compute the optimal power management cost function and policy. This algorithm consists of two successive steps, namely, policy evaluation

This article has been accepted for inclusion in a future issue of this journal. Content is final as presented, with the exception of pagination.

MOURA *et al.*: BATTERY-HEALTH CONSCIOUS POWER MANAGEMENT IN PHEVs   9

and policy improvement, repeated iteratively until convergence. For each possible PHEV state, the policy iteration step approximates the corresponding "cost-to-go" J, which may be intuitively interpreted as the expected cost function value averaged over a stochastic distribution of drive cycles starting at that state. The policy improvement step then approximates the optimal control policy g^*, corresponding to each possible PHEV state. This process iterates until convergence. More details on the implementation of this algorithm can be found in [30]. The following sections present the policy iteration and policy improvement steps in further detail.

1) Policy Evaluation: The policy evaluation step computes the cost-to-go for each state vector value, x, given a control policy, g. This computation is performed recursively as shown in (48)

$$J_{n+1}(x) = c(x, u) + \mathrm{E}_a\left[J_n(f(x, u))\right]. \tag{48}$$

The cost-to-go J is guaranteed to be finite because the system will reach the absorbing state (i.e., vehicle-off) in finite-time with probability one and incur zero cost henceforth. The expectation is taken over vehicle acceleration a, whose dynamics are governed by a Markov chain representing drive cycle behavior (see Section II-E). The index n in the above *recurrence relation* represents an iteration number, and the recurrence relation is evaluated iteratively for all state vector values in the discretized set of admissible states, X. In general, the cost-to-go values within the expectation operator must be interpolated because $f(x, u)$ will never generate the exact values in the discrete-valued state set X. The true cost-to-go for a given control policy must satisfy $J_n = J_{n+1}$. As such, we iterate (48) until one of the two possible conditions are satisfied: 1) the infinity-norm of the normalized difference between J_n and J_{n+1} fall below a threshold value and 2) a finite number of iterations are reached. This truncated policy evaluation approach, used in combination with the policy improvement step below, converges to the optimal control policy regardless of the maximum number of iterations. See [47] for the theory underlying this method.

2) Policy Improvement: Bellman's principle of optimality indicates that the optimal control policy for the stochastic dynamic programming problem in (29)–(32) is also the control policy that minimizes the cost-to-go function $J(x)$ in (48). Thus, to find this control policy u^*, we minimize cost-to-go over all admissible controls for a given state $U(x)$ for each state vector value x, given the cost-to-go function $J(x)$. Mathematically, this minimization is represented by

$$u^*(x) = \arg \min_{u \in U(x)} \left\{ c(x, u) + \mathrm{E}_a[J(x)] \right\}. \tag{49}$$

Equation (49) imposes the state and control input set constraints from Section III-B by minimizing over the admissible control set $U(x)$.

After both policy evaluation and policy improvement are completed, the optimal control policy is passed back into the policy evaluation step and the entire procedure is repeated iteratively. The process terminates when the infinity norm of the difference between two consecutive steps is less than 1%, for both the cost and control functions.
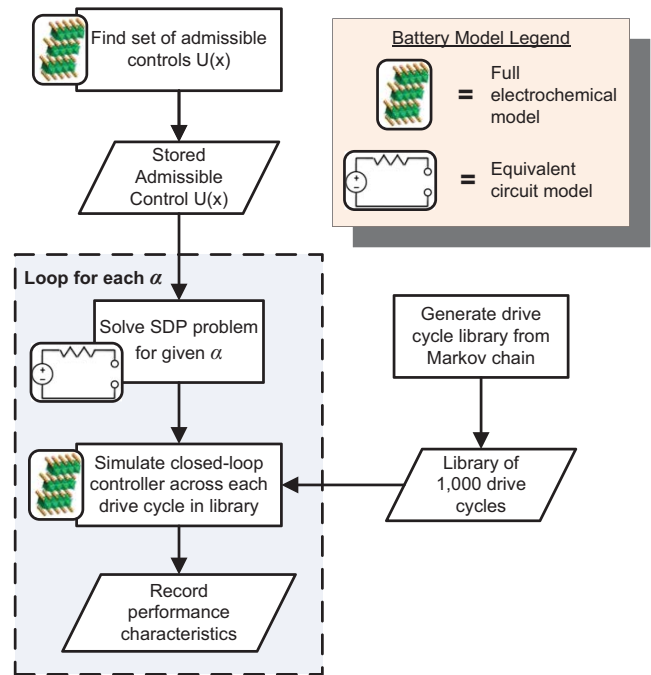

Fig. 6.   Flowchart of the design and analysis procedure. Note that the full electrochemical model is used to compute the admissible control set and simulate the closed-loop system after the SDP problem has been solved. The reduced equivalent circuit model is used to solve the SDP problem, since it contains only one state.

IV. CONTROL SYNTHESIS AND ANALYSIS PROCEDURE

This section examines the performance of supervisory control algorithms that optimally tradeoff battery aging with energy consumption cost. To obtain a measure of controller performance across a variety of drive cycle behavior (as opposed to single certification cycles), we apply the process outlined in Fig. 6. This can be summarized as follows.

1) The set of admissible controls is determined for each state using the electrochemical model.
2) The Pareto optimal set of controllers is synthesized via the stochastic dynamic program formulated in Section III by sweeping α and considering the reduced equivalent circuit model.
3) A library of 1000 drive cycles is generated from the Markov chain described in Section II-E.
4) Each controller in the Pareto set is simulated for all drive cycles in the library with the full electrochemical model.
5) Performance characteristics, including battery-health metrics and energy cost, are recorded.

Subsequently, we analyze three controllers, of interest, from the Pareto set on single certification cycles to obtain a fundamental understanding of how to optimally tradeoff battery-health and energy consumption through proper SoC management.

At this point we wish to highlight Step 1, where the set of admissible controls is determined for each state using the electrochemical model. This step is critical for three reasons.

First, computing admissible controls for each state offline guarantee that the constraints are always satisfied. In other words, they are implemented as *hard* constraints. A typical

This article has been accepted for inclusion in a future issue of this journal. Content is final as presented, with the exception of pagination.

10

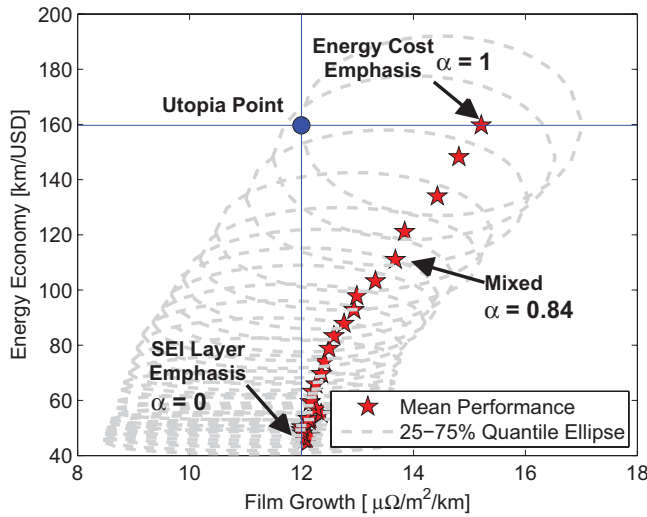IEEE TRANSACTIONS ON CONTROL SYSTEMS TECHNOLOGY

Fig. 7. Pareto set of optimal controllers for anode-side film growth and energy economy, simulated across a library of 1000 randomly generated drive cycles. Stars ($\star$) indicate the average values and the dashed lines (- -) are the 25/75% quantile range.
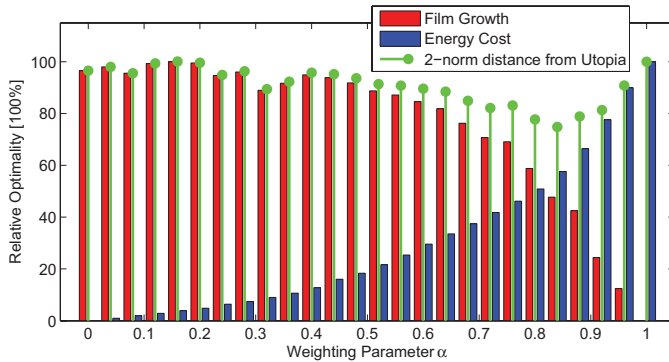

Fig. 8. Relative optimality of each controller depicted in Fig. 7 with respect to each individual objective. The stems are proportional to the two-norm distance from the Utopia point in Fig. 7.

TABLE III
PERFORMANCE OVER VARIOUS CERTIFICATION CYCLES

Drive cycle	Energy economy [km/USD]			Film growth [$\mu\Omega/m^2/km$]		
	SEI $\alpha = 0.00$	Mixed $\alpha = 0.84$	Energy $\alpha = 1.00$	SEI $\alpha = 0.00$	Mixed $\alpha = 0.84$	Energy $\alpha = 1.00$
$3 \times$ FTP	46.5	187	434	14.0	17.9	22.4
$3 \times$ US06	37.1	80.7	88.3	5.25	6.01	6.58
$6 \times$ SC03	50.0	170	312	13.2	16.2	20.0
$3 \times$ HWFET	44.9	173	266	5.15	6.48	7.96
$3 \times$ LA92	39.6	150	263	10.6	13.0	16.2

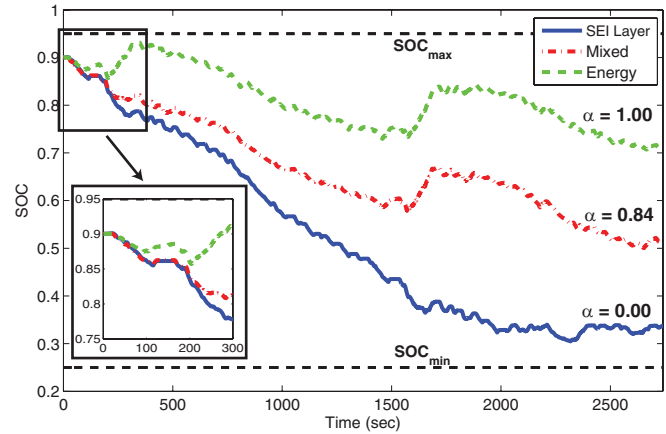Fig. 9. SoC trajectories for SEI film growth ($\alpha = 0$), mixed ($\alpha = 0.84$), and energy ($\alpha = 1.0$) optimal controllers simulated on two concatenated FTP-72 cycles.

V. OPTIMAL BLENDING TO MINIMIZE SEI LAYER

A. Energy Consumption Versus Film Growth

Performance results for the Pareto set of controllers that optimally tradeoff SEI layer film growth (per battery cell) with energy consumption costs are presented in Fig. 7. This is achieved by sweeping the weighting parameter α in (34) from zero to one. A distribution of performance metrics is obtained for simulating the controllers across the entire library of drive cycles. As such, Fig. 7 indicates the average values as well as the 25/75% quantile ranges. The horizontal axis reports the SEI layer growth resistance per km, while the vertical axis indicates energy economy in km/USD (analogous to miles per gallon). The utopia point is located in the upper-left, which indicates the individually achievable optimal performance metrics [53].

This plot indicates that, indeed, there exists a fundamental tradeoff between anode-side SEI film growth in battery packs and energy consumption costs. Namely, average SEI film growth can be reduced by 20% relative to an "energy-only" controller, but at the sacrifice of a 72% decrease in average energy economy. The reason for the distributions of film growth stretch left of the mean is related to the distribution of trip length. As trips become longer, more battery SoC is depleted and film growth rate decreases. Normalizing this effect against longer distances traveled produces a long tail toward the left side of Fig. 7.

alternative in hybrid vehicle power management applications is to apply penalty functions when constraints are violated - a *soft* constraint approach [20], [21], [29]. The latter has been shown to cause numerical difficulties due to the interpolation leakage of the penalty function values into the admissible region [52].

The second critical reason for computing admissible controls offline is that it ensures the controllers satisfy the constraints on the full electrochemical model, despite being optimized on the reduced equivalent circuit model. This point is crucial for integrating electrochemical models into stochastic dynamic programming - a key contribution of this paper.

Finally, computing admissible controls offline can dramatically reduce the control space, one needs to consider during the online SDP calculation. For the results provided in this paper, 86% of the control space was eliminated.

The results from computing the admissible controls are saved into a database, which SDP uses to determine the set over which to optimize controls for each state. This offline calculation does not depend on the specific optimization objective, and can thus be performed once. As such, the database of admissible controls is used to minimize SEI layer growth and Ah-processed in the subsequent sections.

This article has been accepted for inclusion in a future issue of this journal. Content is final as presented, with the exception of pagination.

MOURA *et al.*: BATTERY-HEALTH CONSCIOUS POWER MANAGEMENT IN PHEVs   11
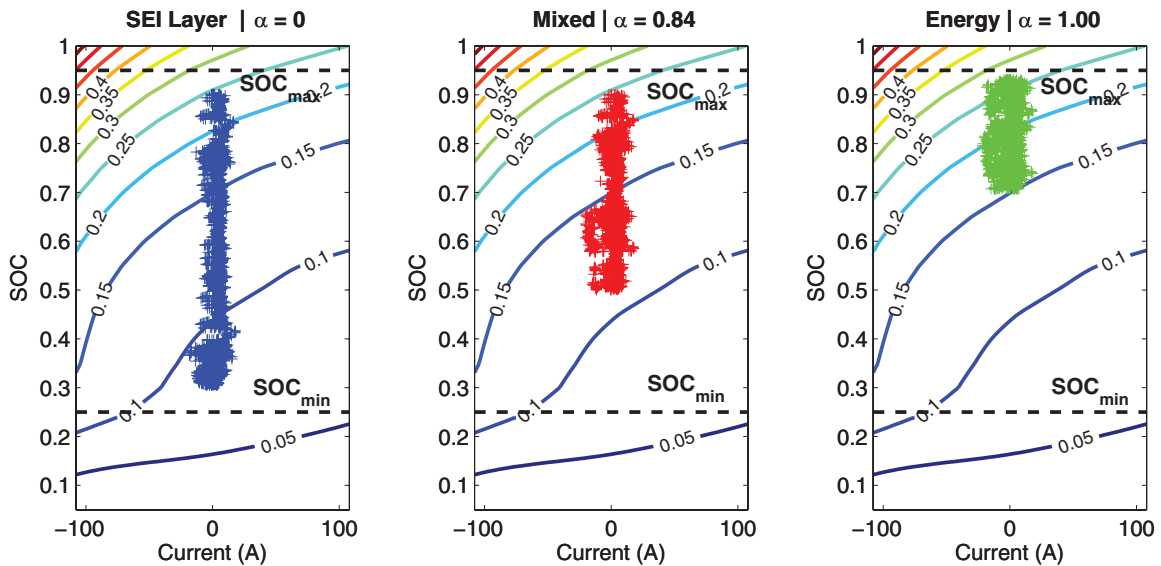
Fig. 10.   Operating points on anode-side SEI film growth rate map for SEI layer ($\alpha = 0$), mixed ($\alpha = 0.84$), and energy ($\alpha = 1.0$) optimal controllers simulated on two concatenated FTP-72 cycles.

One method for analyzing the combined optimality of each controller is to consider the relative optimality analysis depicted in Fig. 8. This figure reports on the optimality of each controller with respect to the Utopia point defined in Fig. 7. Note that the relative optimality is nearly (but not exactly) a monotonic function of controller weighting α. This is because the stochastic dynamic programming procedure optimizes with respect to the reduced-order equivalent circuit battery model, whereas these results are calculated from the full electrochemical model (see Fig. 6). One can see that the controller corresponding to $\alpha = 0.84$ provides the minimum two-norm distance from the Utopia point, and in this specific sense, is the best balance between both objectives. In the following analysis, we discuss the two extreme solutions ($\alpha = 0$ and $\alpha = 1$) and the "best mix" ($\alpha = 0.84$).

B. Analysis and Discussion

To acquire physical insight into the structural properties of the optimal controllers, we analyze three solutions from the Pareto set, $\alpha = 1.0, 0.84$, and 0. Generally speaking these, respectively, correspond to emphasizing energy only, balancing energy and SEI layer growth, and SEI layer growth only. The controller corresponding to $\alpha = 0.84$ is chosen because it represents the best balance between both objectives, measured in terms of the normalized two-norm distance from the utopia point in Fig. 7. These controllers are simulated on two concatenated FTP-72 cycles, which produces performance characteristics representative of the extreme behavior. Performance results for various other drive cycles are reported in Table III.

Fig. 9 demonstrates the SoC trajectories for each controller. The energy-only controller ($\alpha = 1.0$) conservatively rations battery charge by blending engine and battery power. This process reduces the time spent in charge sustenance mode, where fuel must be consumed to meet power demand and sustain battery charge [2]. Put simply, charge sustenance mode

is extremely expensive relative to charge depletion, and should be avoided, if possible, to reduce energy consumption cost. If the drive cycle was known beforehand, the optimal strategy would blend engine and battery power so battery SoC reaches its minimum level exactly when the trip terminates. Recall that trip length distributions are directly implemented into the problem formulation through the terminal state of the Markov chain, as described in Section II-E. Hence the controller is trip length-conscious. In contrast, the SEI layer-only controller ($\alpha = 0$) aggressively depletes battery charge to avoid the high SEI film growth rates seen in Fig. 3. This results in a strategy that mimics electric-only operation, followed by charge sustenance. Interestingly, the mixed ($\alpha = 0.84$) controller's characteristics are more similar to $\alpha = 0$ than $\alpha = 1$ during the first 300 seconds (see the zoom-in in Fig. 9). The reason can be understood by analyzing the gradient properties of the film growth map. Namely, the steep gradient at high SoC values indicates significant benefits in accumulated film growth can be achieved by quickly depleting charge. This is in spite of heavily weighting energy costs over battery-health, since instantaneous energy cost as defined in (35) is relatively insensitive to SoC. Conversely, SEI film growth is very sensitive to SoC. Mathematically, this is shown from (35) and (36)

$$\frac{\partial c_H}{\partial \mathrm{SoC}} \gg \frac{\partial c_E}{\partial \mathrm{SoC}} \tag{50}$$

$$\Leftrightarrow \frac{\partial \dot{\delta}_{\mathrm{film}}(I, \mathrm{SoC})}{\partial \mathrm{SoC}} \gg -\frac{Q_{\mathrm{batt}}\dot{\mathrm{SoC}}}{\eta_{\mathrm{EVSE}}}\frac{dV_{\mathrm{oc}}(\mathrm{SoC})}{d\mathrm{SoC}} \approx 0 \tag{51}$$

where the RHS of (51) is approximately zero because a typical Li-ion battery has nearly constant open-circuit voltage with respect to SoC, in the allowable SoC range.

This result is clearly illustrated in Fig. 10, which indicates the operating points of each controller superimposed on the film growth map from Fig. 3. Observe that adding a small consideration for SEI layer growth (e.g., $\alpha = 0.84$) to an energy-only objective (e.g., $\alpha = 1.0$) dramatically changes

This article has been accepted for inclusion in a future issue of this journal. Content is final as presented, with the exception of pagination.

12   IEEE TRANSACTIONS ON CONTROL SYSTEMS TECHNOLOGY
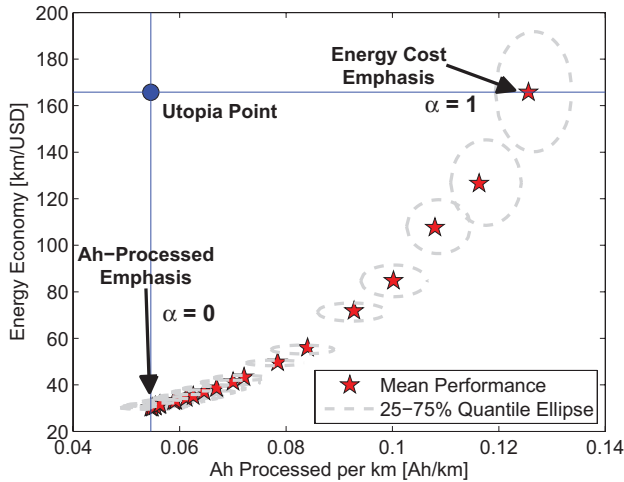

Fig. 11.   Pareto set of optimal controllers for Ah processed and energy economy, simulated across a library of 1000 randomly generated drive cycles. Stars (⋆) indicate the average values and the dashed lines (- -) are the 25/75% quantile range.

the operating point behavior. Namely, it induces the controller to escape high-film growth rate regions by depleting battery charge quickly until it reaches a lower SoC level (between 50–60%). However, it leaves enough available battery energy to blend power until the trip ends, without entering charge sustenance (near 25% SoC). In summary, a PHEV power management strategy that considers SEI film growth in addition to energy consumption will, in general: 1) deplete battery charge quickly to reduce film growth rates and 2) blend engine and battery power to avoid charge sustenance, at least for the models considered in this paper.

The property that batteries degrade faster at higher SoC influences the results presented here. Experimental validation of this result has been reported several times in the literature [44], [54], [55]. Moreover, analysis of the physics-based models reveals this property is true if and only if the anode equilibrium potential decreases with bulk anode SoC, which is a thermodynamic property of lithiated carbon electrodes [56]. In this paper, we focus on one particular battery degradation mechanism - anode-side film growth. In truth, a myriad of mechanisms exists that cause capacity fade in lithium-ion batteries, although film growth has been identified as one of the most significant [6]. A comprehensive review of these mechanisms can be found in [6] and the references therein. From a systems-level perspective, degradation can be associated with SoC, temperature, depth of discharge, cycling, etc. Experiments identifying several of these relationships are currently underway in our laboratory. Nonetheless, the key contribution of this paper is to elucidate how the mathematical structure of health degradation dynamics relates to enhanced battery-health conscious power management in PHEVs.

VI. Optimal Blending to Minimize Ah-Processed

In this section, we examine the performance of supervisory control algorithms that optimally tradeoff Ah processed with energy consumption cost. The analysis follows the exact same procedure outlined in the previous section (Section V) and
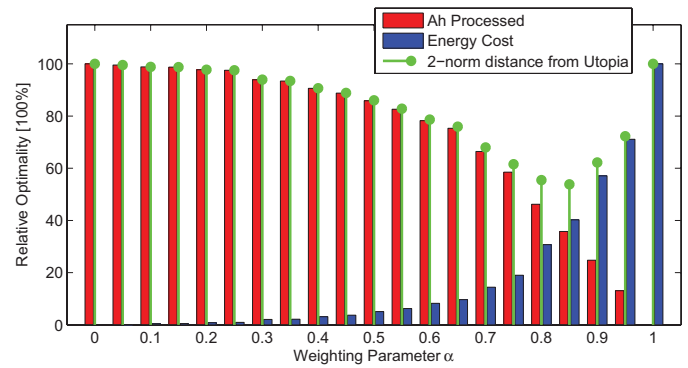

Fig. 12.   Relative optimality of each controller depicted in Fig. 11 with respect to each individual objective. The stems are proportional to the two-norm distance from the Utopia point in Fig. 11.

Fig. 6. In particular, we analyze the Pareto frontier of optimal solutions and their relative optimality. For additional insight, we consider the controllers that optimize each objective individually and compare their performance on three concatenated US06 cycles, which produces performance characteristics representative of the extreme behavior.

A. Energy Consumption Versus Ah Processed

Performance results for the Pareto set of controllers that optimally tradeoff Ah processed (per battery cell) with energy consumption costs are presented in Fig. 11. As before, this is achieved by sweeping the weighting parameter α in (34) from zero to one. A distribution of performance metrics is obtained for simulating the controllers across the entire library of drive cycles. As such, Fig. 7 indicates the average values as well as the 25/75% quantile ranges. The horizontal axis reports the Ah processed per km, while the vertical axis indicates energy economy in km/USD (analogous to miles per gallon). The utopia point is located in the upper-left, which indicates the individually achievable optimal performance metrics [53].

This plot indicates that a fundamental tradeoff also exists between reducing energy consumption costs and Ah processed in battery packs, for PHEVs. Specifically, the average Ah processed can be reduced by 57% relative to an "energy-only" controller, but at the sacrifice of an 82% decrease in average energy economy. One method for analyzing the combined optimality of each controller is to consider the relative optimality analysis depicted in Fig. 12. This figure reports on the optimality of each controller with respect to the Utopia point defined in Fig. 11. One can see that the controller corresponding to $\alpha = 0.85$ provides the minimum two-norm distance from the Utopia point, and in this specific sense, is the best balance between both objectives.

B. Analysis and Discussion

As before, we acquire physical insight into the structural properties of the optimal controllers by analyzing the three solutions from the Pareto set, $\alpha = 0, 0.85$ 1.0. These three controllers correspond to emphasizing minimum Ah-processed, balanced Ah-processed and energy, and minimum energy
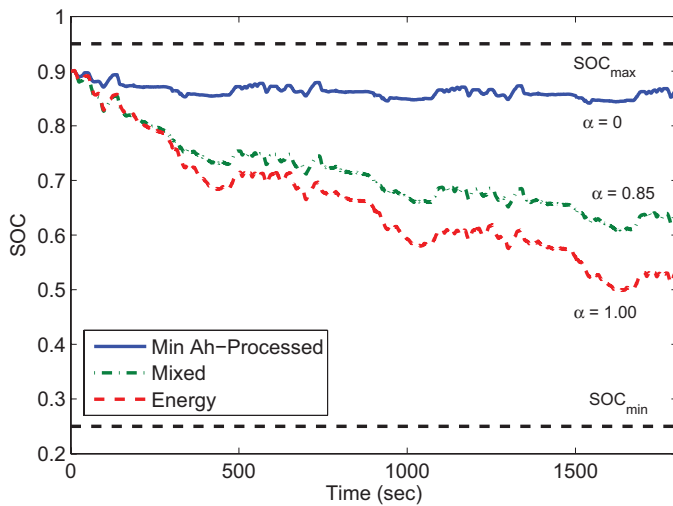
This article has been accepted for inclusion in a future issue of this journal. Content is final as presented, with the exception of pagination.

MOURA *et al.*: BATTERY-HEALTH CONSCIOUS POWER MANAGEMENT IN PHEVs 13

Fig. 13. SoC trajectories for minimum Ah-processed ($\alpha = 0$) and energy ($\alpha = 1.0$) simulated on three concatenated US06 cycles.
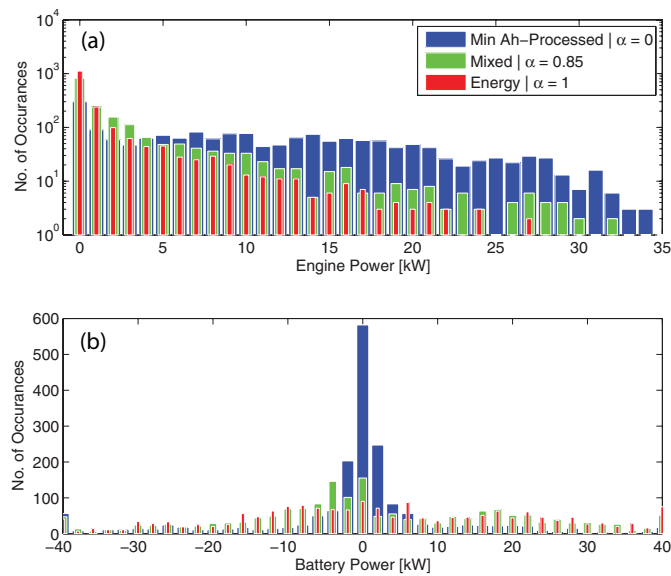

Fig. 14. Distributions of (a) engine and (b) battery power for minimum Ah-processed ($\alpha = 0$) and energy ($\alpha = 1.0$) simulated on three concatenated US06 cycles.

consumption cost, respectively. These controllers are simulated on three concatenated US06 cycles.

Fig. 13 portrays the SoC trajectories for each controller. As before, the energy-focused controller rations battery charge such that the PHEV reaches the minimum SoC over the course of an average drive cycle. This effectively reduces the time spent in charge sustenance mode, while completely utilizing the relatively cheap electric energy store. In contrast to the results shown in Fig. 9, the minimum Ah-processed controller severely limits high C-rates and therefore consumes a very small amount of battery energy (about 5% depth of discharge).

This behavior can be understood further by analyzing the distribution of power demand on the engine and battery, depicted in Fig. 14(a) and (b). This figure elucidates how the minimum Ah-processed controller constraints the distribution of battery power demand to a small range around 0 kW, which

limits the depth of discharge. The tradeoff is a larger number of high engine power occurrences, as shown in Fig. 14(a), to satisfy the total power demand. In contrast, the energy-focused controller experiences a broad range of battery power demand and a distribution of engine power more closely concentrated toward lower values, which decreases total energy consumption cost. Therefore, a PHEV supervisory control algorithm that attempts to minimize the battery-health degradation by reducing Ah-processed will be extremely cautious of using the battery as a depletable energy store. Interestingly, this action fundamentally opposes the key advantageous feature of a PHEV - the depletable battery pack energy store.

VII. CONCLUSION

This paper develops techniques for the health-conscious power management in PHEVs through electrochemical modeling and stochastic control. Namely, we formulate a multiobjective optimal control problem that optimally trades-off battery-health with energy consumption cost (fuel and grid electricity). The two battery-health metrics examined here include anode-side resistive film formation and Ah processed. In addition, we apply a shortest-path stochastic dynamic programming formulation. This enables us to match the Markov chain drive cycle model with real-world daily trip length distributions reported by the National Household Travel Survey [46].

The main objective of this paper is to *develop a framework* for designing battery-health optimized supervisory controllers. To demonstrate this framework, we apply it to two existing battery degradation models in the literature - one based upon theoretical principles (SEI layer) and the other upon experimental data (Ah processed). Nonetheless, the concepts are broadly applicable to other degradation models/metrics, e.g., lithium plating [34], temperature [40], mechanical stress [10], and empirical relations based upon experimental data [15]. We note that the degradation case studies provided in this paper have two simplifying properties: 1) they do not add state-variables and 2) they only require signals from an equivalent circuit model. The critical challenge of incorporating other aging mechanisms is overcoming the curse of dimensionality associated with dynamic programming.

Our case studies demonstrate that a health-optimized strategy for minimizing SEI-layer or Ah-processed will, respectively, deplete battery charge quickly or ration it conservatively. This contradiction underscores the importance of developing accurate, experimentally-validated, yet control-oriented health degradation models in future work. Complicating this effort is that varying material designs, charge/discharge loads, environmental conditions, and manufacturing processes can greatly affect battery degradation properties. As such, a useful extension might consider adaptive schemes [57], [58] that identify degradation dynamics online and adjust the control strategy accordingly. Nonetheless, the methods developed here provide the fundamental techniques to integrate battery-health models with optimal control to design the power management algorithms.

This article has been accepted for inclusion in a future issue of this journal. Content is final as presented, with the exception of pagination.

14   IEEE TRANSACTIONS ON CONTROL SYSTEMS TECHNOLOGY

APPENDIX

NOMENCLATURE

PHEV

A_{fr}	Effective frontal area of vehicle,	[m^2]
a	Vehicle acceleration,	[m/s^2]
C_d	Aerodynamic drag coefficient	
F_g	Planetary gear force,	[N]
I_e	Engine inertia,	[kg·m^2]
I_{M1}	Machine 1 inertia,	[kg·m^2]
I_{M2}	Machine 2 inertia,	[kg·m^2]
I_w	Wheel inertia,	[kg·m^2]
K	Final drive ratio	
m	Vehicle mass,	[kg]
R	Number of teeth on ring gear	
R_{tire}	Tire radius,	[m]
S	Number of teeth on sun gear	
T_e	Engine torque,	[N·m]
T_{M1}	Machine 1 torque,	[N·m]
T_{M2}	Machine 2 torque,	[N·m]
υ	Vehicle speed,	[m/s]
η_{M1}	M1 power efficiency	
η_{M2}	M2 power efficiency	
μ_{roll}	Rolling friction coefficient	
ρ	Air density,	[kg/m^3]
ω_e	Engine crankshaft speed,	[rad/s]
ω_{M1}	Machine 1 speed,	[rad/s]
ω_{M2}	Machine 2 speed,	[rad/s]

BATTERY

a_n	Specific surface area of anode,	[m^2/m^3]
A	Cell sheet surface area,	[m^2]
c_1, c_2	Ion concentration in solid, electrolyte,	[moles/m^3]
D_1, D_2	Diffusion coefficient in solid, electrolyte,	[m^2/s]
F	Faraday's constant,	[C/mol]
I	Current through each cell,	[A]
i_0	Battery pack current,	[A]
$i_{0,s}$	Exchange current density for side reaction,	[A/m^2]
J	Intercalation current density,	[A/m^3]
J_{sd}	Current density of side reaction,	[A/m^3]
M_P	Molecular weight of product from side reaction,	[mol/kg]
n_p	No. of parallel strings of cells	
n_s	No. of cells in series per string	
P_{batt}	Power transfer from batt pack,	[W]
Q_{batt}	Battery pack charge capacity,	[A·s]
r	Radial coordinate in solid particles,	[m]
R_{gas}	Universal gas constant,	[J/K/mol]
R_{batt}	Internal resistance of batt pack,	[Ω]
R_{film}	Total film resistance,	[Ω/m^2]
R_{SEI}	Resistance of solid electrolyte interphase (SEI),	[Ω/m^2]
SoC	Battery state of charge	
t^+	Transference number	

$U_{\text{ref},j}$	Equilibrium potential of solid,	[V]
$U_{\text{ref},s}$	Equilibrium potential of side reaction,	[V]
V_{cell}	Voltage of individual cell,	[V]
V_{oc}	Batt. pack open circuit voltage,	[V]
x	Spatial coordinate across cell,	[m/m]
$\overline{(\delta_{\text{film}})}$	(Spatially averaged) anode-side	
δ_{film}	SEI resistive film thickness,	[pm/m^2]
η_{sd}	Side reaction overpotential,	[V]
$\kappa^{\text{eff}}, \kappa$	Conductivity of electrolyte,	[1/m/Ω]
κ_P	Conductivity of SEI product,	[1/m/Ω]
ρ_P	Side reaction product density,	[kg/m^2]
σ^{eff}	Effective solid conductivity,	[1/m/Ω]
ϕ_1, ϕ_2	Solid, electrolyte potential,	[V]

OPTIMIZATION

$c(\cdot, \cdot)$	Instantaneous cost function	
J^g	Optimal cost for control policy g	
SoC$_{\text{cs}}$	Charge sustaining SoC level	
$U(x)$	Admissible set of controls	
W_{fuel}	Mass flow rate of fuel,	[g/s]
X	Admissible set of states	
α	Linear weight	
β	Energy price ratio, USD/USD	
η_{EVSE}	EV supply equip. chg. efficiency	

ACKNOWLEDGMENT

REFERENCES

[1] V. Ramadesigan, P. W. C. Northrop, S. De, S. Santhanagopalan, R. D. Braatz, and V. R. Subramanian, "Modeling and simulation of lithium-ion batteries from a systems engineering perspective," *J. Electrochem. Soc.*, vol. 159, no. 3, pp. R31–R45, 2012.

[2] S. J. Moura, H. K. Fathy, D. S. Callaway, and J. L. Stein, "A stochastic optimal control approach for power management in plug-in hybrid electric vehicles," *IEEE Trans. Control Syst. Technol.*, vol. 19, no. 3, pp. 545–555, May 2011.

[3] S. J. Moura, J. L. Stein, and H. K. Fathy, "Battery health-conscious power management for plug-in hybrid electric vehicles via stochastic control," in *Proc. ASME Dyn. Syst. Control Conf.*, 2010, pp. 1–2.

[4] S. J. Moura, J. C. Forman, J. L. Stein, and H. K. Fathy, "Control of film growth in lithium ion battery packs via switches," in *Proc. ASME Dyn. Syst. Control Conf.*, 2009, pp. 1–9.

[5] P. Ramadass, B. Haran, P. Gomadam, R. White, and B. Popov, "Development of first principles capacity fade model for Li-ion cells," *J. Electrochem. Soc.*, vol. 151, no. 2, pp. 196–203, 2004.

[6] D. Aurbach, "Review of selected electrode-solution interactions which determine the performance of Li and Li ion batteries," *J. Power Source*, vol. 89, no. 2, pp. 206–218, 2000.

[7] R. Bhattacharyya, B. Key, H. Chen, A. S. Best, A. F. Hollenkamp, and C. P. Grey, "In situ NMR observation of the formation of metallic lithium microstructures in lithium batteries," *Nature Mater.*, vol. 9, no. 6, pp. 504–510, 2010.

This article has been accepted for inclusion in a future issue of this journal. Content is final as presented, with the exception of pagination.

MOURA *et al.*: BATTERY-HEALTH CONSCIOUS POWER MANAGEMENT IN PHEVs

15

[8] W. Gu and C. Wang, "Thermal-electrochemical modeling of battery systems," *J. Electrochem. Soc.*, vol. 147, no. 8, pp. 2910–2922, 2000.

[9] J. Christensen, "Modeling diffusion-induced stress in Li-ion cells with porous electrodes," *J. Electrochem. Soc.*, vol. 157, no. 3, pp. A366–A380, 2010.

[10] R. Deshpande, Y.-T. Cheng, M. W. Verbrugge, and A. Timmons, "Diffusion induced stresses and strain energy in a phase-transforming spherical electrode particle," *J. Electrochem. Soc.*, vol. 158, no. 6, pp. A718–A724, Apr. 2011.

[11] K. Hatzell, A. Sharma, and H. Fathy, "A survey of long-term health modeling, estimation, and control challenges and opportunities for lithium-ion batteries," in *Proc. 2012 Amer. Control Conf.*, Montreal, QC, Canada, 2012.

[12] M. Doyle, T. Fuller, and J. Newman, "Modeling of galvanostatic charge and discharge of the lithium/polymer/insertion cell," *J. Electrochem. Soc.*, vol. 140, no. 6, pp. 1526–1533, 1993.

[13] T. Fuller, M. Doyle, and J. Newman, "Simulation and optimization of the dual lithium ion insertion cell," *J. Electrochem. Soc.*, vol. 141, no. 1, pp. 1–10, 1994.

[14] S. B. Peterson, J. Apt, and J. Whitacre, "Lithium-ion battery cell degradation resulting from realistic vehicle and vehicle-to-grid utilization," *J. Power Source*, vol. 195, no. 8, pp. 2385–2392, 2010.

[15] J. Wang, P. Liu, J. Hicks-Garner, E. Sherman, S. Soukiazian, M. Verbrugge, H. Tataria, J. Musser, and P. Finamore, "Cycle-life model for graphite-LiFePO$_4$ cells," *J. Power Source*, vol. 196, no. 8, pp. 3942–3948, 2011.

[16] C. Musardo, G. Rizzoni, Y. Guezennec, and B. Staccia, "A-ECMS: An adaptive algorithm for hybrid electric vehicle energy management," *Eur. J. Control*, vol. 11, nos. 4–5, pp. 509–524, 2005.

[17] A. Vahidi, A. Stefanopoulou, and H. Peng, "Current management in a hybrid fuel cell power system: A model-predictive control approach," *IEEE Trans. Control Syst. Technol.*, vol. 14, no. 6, pp. 1047–1057, Nov. 2006.

[18] Q. Gong, Y. Li, and Z.-R. Peng, "Trip-based optimal power management of plug-in hybrid electric vehicles," *IEEE Trans. Veh. Technol.*, vol. 57, no. 6, pp. 3393–3401, Nov. 2008.

[19] M. P. O'Keefe and T. Markel, "Dynamic programming applied to investigate energy management strategies for a plug-in HEV," in *Proc. 22nd Int. Battery, Hyb. Fuel Cell Elect. Veh. Symp.*, Oct. 2006, pp. 1–15.

[20] C.-C. Lin, "Modeling and control strategy development for hybrid vehicles," Ph.D. dissertation, Dept. Electr. Eng. Comput. Sci., Univ. Michigan, Ann Arbor, 2004.

[21] D. Kum, H. Peng, and N. Bucknor, "Modeling and control of hybrid electric vehicles for fuel and emission reduction," in *Proc. ASME Dyn. Syst. Control Conf.*, 2008, pp. 1247–1254.

[22] D. F. Opila, D. Aswani, R. McGee, J. A. Cook, and J. W. Grizzle, "Incorporating drivability metrics into optimal energy management strategies for hybrid vehicles," in *Proc. 47th IEEE Conf. Decision Control*, Dec. 2008, pp. 4382–4389.

[23] M. Amiri, M. Esfahanian, M. R. Hairi-Yazdi, and V. Esfahanian, "Minimization of power losses in hybrid electric vehicles in view of the prolonging of battery life," *J. Power Source*, vol. 190, no. 2, pp. 372–379, 2009.

[24] N. Shidore, J. Kwon, and A. Vyas, "Trade-off between PHEV fuel efficiency and estimated battery cycle life with cost analysis," in *Proc. 5th IEEE Veh. Power Propulsion Conf.*, Sep. 2009, pp. 669–677.

[25] Z. Amjadi and S. S. Williamson, "Power-electronics-based solutions for plug-in hybrid electric vehicle energy storage and management systems," *IEEE Trans. Ind. Electron.*, vol. 57, no. 2, pp. 608–616, Feb. 2010.

[26] C. Mi, B. Li, D. Buck, and N. Ota, "Advanced electro-thermal modeling of lithium-ion battery system for hybrid electric vehicle applications," in *Proc. IEEE Veh. Power Propulsion Conf.*, Sep. 2007, pp. 107–111.

[27] K. Muta, M. Yamazaki, and J. Tokieda, "Development of new-generation hybrid system THS II - drastic improvement of power performance and fuel economy," in *Proc. SAE World Congr.*, 2004, Art No. 2004-01-0064, p. 0064.

[28] *2012 Toyota Plug-In Prius Review Popular Mechanics*. (2009) [Online]. Available: http://www.popularmechanics.com/automotive/new_cars/4339705.html

[29] J. Liu, "Modeling, configuration and control optimization of power-split hybrid vehicles," Ph.D. dissertation, Dept. Mech. Eng., Univ. Michigan, Ann Arbor, 2007.

[30] S. J. Moura, "Techniques for battery health conscious power management via electrochemical modeling and optimal control," Ph.D. dissertation, Dept. Mech. Eng., Univ. Michigan, Ann Arbor, 2011.

[31] A. Rousseau, J. Kwon, P. Sharer, and M. Duoba, "Integrating data, performing quality assurance, and validating the vehicle model for the 2004 prius using PSAT," SAE, Warrendale, PA, Tech. Rep. 2006-01-0667, 2006.

[32] *High Power Lithium Ion ANR26650M1 Data Sheet*, A123 Systems, Waltham, MA, 2006.

[33] J. C. Forman, S. J. Moura, J. L. Stein, and H. K. Fathy, "Parameter identification of the Doyle-Fuller-Newman model based on experimental cycling of a li-ion LiFePO$_4$ battery using a genetic algorithm," in *Proc. Amer. Control Conf.*, 2011, pp. 1–8.

[34] N. A. Chaturvedi, R. Klein, J. Christensen, J. Ahmed, and A. Kojic, "Algorithms for advanced battery-management systems," *IEEE Control Syst. Mag.*, vol. 30, no. 3, pp. 49–68, Jun. 2010.

[35] K. Smith, C. Rahn, and C.-Y. Wang, "Model-based electrochemical estimation of lithium-ion batteries," in *Proc. IEEE Int. Conf. Control Appl.*, Sep. 2008, pp. 714–719.

[36] S. Santhanagopalan, Q. Zhang, K. Kumaresan, and R. White, "Parameter estimation and life modeling of lithium-ion cells," *J. Electrochem. Soc.*, vol. 155, no. 4, pp. 345–353, Apr. 2008.

[37] D. D. Domenico, A. Stefanopoulou, and G. Fiengo, "Lithium-ion battery state of charge and critical surface charge estimation using an electrochemical model-based extended Kalman filter," *J. Dyn. Syst., Meas., Control*, vol. 132, no. 6, pp. 061302-1–061302-11, Nov. 2010.

[38] J. C. Forman, S. Bashash, J. L. Stein, and H. K. Fathy, "Reduction of an electrochemistry-based Li-ion battery degradation model via quasi-linearization and pade approximation," *J. Electrochem. Soc.*, vol. 158, no. 2, pp. A93–A101, 2011.

[39] A. Baughman and M. Ferdowsi, "Battery charge equalization-state of the art and future trends," SAE, Warrendale, PA, Tech. Rep. 2005-01-3474, 2005.

[40] W. Fang, O. J. Kwon, and C.-Y. Wang, "Electrochemical-thermal modeling of automotive Li-ion batteries and experimental validation using a three-electrode cell," *Int. J. Energy Res.*, vol. 34, no. 2, pp. 107–115, 2010.

[41] P. Nelson, D. Dees, K. Amine, and G. Henriksen, "Modeling thermal management of lithium-ion PNGV batteries," *J. Power Source*, vol. 110, no. 2, pp. 349–356, 2002.

[42] C. Forgez, D. V. Do, G. Friedrich, M. Morcrette, and C. Delacourt, "Thermal modeling of a cylindrical LiFePO$_4$/graphite lithium-ion battery," *J. Power Source*, vol. 195, no. 9, pp. 2961–2968, 2010.

[43] P. Wolf, S. J. Moura, and M. Krstic, "Optimal sensor placement for spatio-temporal temperature estimation in large battery packs," in *Proc. IEEE Conf. Decision Control*, Maui, HI, Dec. 2012.

[44] M. Broussely, P. Biensan, F. Bonhomme, P. Blanchard, S. Herreyre, K. Nechev, and R. Staniewicz, "Main aging mechanisms in Li ion batteries," *J. Power Source*, vol. 146, nos. 1–2, pp. 90–96, 2005.

[45] J. Newman, *Electrochemical Systems*, 2nd ed. Englewood Cliffs, NJ: Prentice-Hall, 1991.

[46] USDOT-FHWA. (2009). *National Household Travel Survey*, Washington, DC [Online]. Available: http://nhts.ornl.gov/index.shtml

[47] D. Bertsekas, *Dynamic Programming and Optimal Control*, vols. 1–2. Belmont, MA: Athena Scientific, 2005.

[48] *Daily Fuel Gauge Report*. (2010) [Online]. Available: http://www.fuelgaugereport.com/

[49] US-DOE. (2010). *Average Retail Price of Electricity to Ultimate Customers by End-Use Sector, by State*, Washington, DC [Online]. Available: http://www.eia.doe.gov/electricity/epm/table5_6_b.html

[50] M. A. Wiering and E. D. De Jong, "Computing optimal stationary policies for multiobjective Markov decision processes," in *Proc. IEEE Symp. Approx. Dyn. Program. Reinf. Learn.*, Apr. 2007, pp. 158–165.

[51] E. Tate, "Techniques for hybrid electric vehicle controller synthesis," Ph.D. dissertation, Dept. Elect. Eng. Syst., Univ. Michigan, Ann Arbor, 2007.

[52] O. Sundstrom, D. Ambuhl, and L. Guzzella, "On implementation of dynamic programming for optimal control problems with final state constraints," *Oil Gas Sci. Technol.*, vol. 65, no. 1, pp. 91–102, 2010.

[53] P. Papalambros and D. Wilde, *Principles of Optimal Design: Modeling and Computation*. Cambridge, U.K.: Cambridge Univ. Press, 2000.

[54] M. Ichimura, M. Shimomura, K. Takeno, R. Shirota, and J.-I. Yamaki, "Synergistic effect of charge/discharge cycle and storage in degradation of lithium-ion batteries for mobile phones," in *Proc. Int. Telecommun. Energy Conf.*, Berlin, Germany, 2005, pp. 245–250.

[55] M.-S. Wu, P.-C. J. Chiang, and J.-C. Lin, "Electrochemical investigations on capacity fading of advanced lithium-ion batteries after storing at elevated temperature," *J. Electrochem. Soc.*, vol. 152, no. 6, pp. A1041–A1046, 2005.

[56] D. Karthikeyan, G. Sikha, and R. White, "Thermodynamic model development for lithium intercalation electrodes," *J. Power Source*, vol. 185, no. 2, pp. 1398–1407, 2008.

[57] S. J. Moura, N. A. Chaturvedi, and M. Krstic, "PDE estimation techniques for advanced battery management systems - Part I: SoC estimation," in *Proc. Amer. Control Conf.*, Montreal, QC, Canada, 2012.

[58] S. J. Moura, N. A. Chaturvedi, and M. Krstic, "PDE estimation techniques for advanced battery management systems - Part II: SOH identification," in *Proc. Amer. Control Conf.*, Montreal, QC, Canada, 2012.

Jeffrey L. Stein is a Full Professor with the Department of Mechanical Engineering, University of Michigan, Ann Arbor, and is the former Chair of the Dynamic Systems and Control Division, American Society of Mechanical Engineers. His expertise is in computer-based modeling and simulation tools for system design and control. His application expertise is in the areas of automotive engineering, including green energy transportation, machine tool designs, and lower leg prosthetics. In green transportation, he is working to develop the techniques for the design and control of plug-in hybrid vehicles and smart grid technologies that creates a more efficient use of energy, particular that generated from renewable resources, for a lower carbon and other emissions footprint. He has authored or co-authored over 150 articles in journals and conference proceedings. His current research interests include algorithms for automating the development of proper dynamic mathematical models (minimum yet sufficient complexity models with physical parameters).

Scott J. Moura (S'09) received the B.S. degree from the University of California, Berkeley, and the M.S. and Ph.D. degrees from the University of Michigan, Ann Arbor, in 2006, 2008, and 2011, respectively, all in mechanical engineering.

He is currently a Post-Doctoral Research Fellow with the Mechanical and Aerospace Engineering Department, University of California San Diego, San Diego. His current research interests include optimal and adaptive controls, partial differential equations control, energy conversion systems, smart grid systems, and batteries.

Dr. Moura was a recipient of the National Science Foundation Graduate Research Fellowship, the UC Presidential Post-Doctoral Fellowship, the University of Michigan Distinguished ProQuest Dissertation Honorable Mention, and the University of Michigan Rackham Merit Fellowship, College of Engineering Distinguished Leadership Award. He has been nominated for the Best Student Paper Award from the American Society of Mechanical Engineers Dynamic Systems and Control Conference in 2009 and the American Control Conference in 2011.

Hosam K. Fathy received the B.Sc. degree from American University, Cairo, Egypt, the M.S. degree from Kansas State University, Manhattan, and the Ph.D. degree from and the University of Michigan, Ann Arbor, in 1997, 1999, and 2003, respectively, all in mechanical engineering.

He was a Control Systems Engineer with Emmeskay, Inc., Plymouth, MI, from 2003 to 2004, and subsequently a Post-Doctoral Research Fellow from 2004 to 2006 and an Assistant Research Scientist from 2006 to 2010 with the University of Michigan. Since 2010, he has been a Mechanical Engineering Assistant Professor with Penn State University, University Park. His Control Optimization Laboratory is active in the fundamental areas of model reduction and optimal control and their application to transportation and energy systems. He has co-authored more than 65 peer-reviewed conference and journal publications in diverse areas, including battery health modeling and control, plug-in hybrid vehicle power management, and demand response for the smart grid.